Atmos. Meas. Tech., 8, 2685–2697, 2015
www.atmos-meas-tech.net/8/2685/2015/
doi:10.5194/amt-8-2685-2015


Atmospheric Measurement Techniques
Open Access

# Impacts of atmospheric state uncertainty on $O_2$ measurement requirements for the ASCENDS mission

**S. Crowell[1], P. Rayner[2], S. Zaccheo[3], and B. Moore[1]**

[1]School of Meteorology, University of Oklahoma, 100 David Boren Blvd, Norman, OK 73072, USA
[2]School of Earth Sciences, University of Melbourne, Melbourne, Australia
[3]Atmospheric and Environmental Research, 131 Hartwell Avenue, Lexington, MA 02421, USA

*Correspondence to:* S. Crowell (scrowell@ou.edu)

Received: 16 May 2014 – Published in Atmos. Meas. Tech. Discuss.: 10 July 2014
Revised: 05 June 2015 – Accepted: 08 June 2015 – Published: 03 July 2015

**Abstract.** Remotely sensed observations of atmospheric composition require an estimate of surface pressure. This estimate can either come from an instrument with sensitivity in an $O_2$ absorption feature in the spectrum, or it can be provided by a numerical weather prediction (NWP) model. In this work, the authors outline an information-based methodology for setting measurement requirements for an active lidar measurement of $O_2$ in the context of the Active Sensing of Carbon Emissions over Nights, Days and Seasons (ASCENDS) mission. The results indicate that the impacts of correlations in the environmentally induced vertical weighting function errors between $CO_2$ and $O_2$ measurements are nontrivial and that the choice of $CO_2$ and $O_2$ wavelengths can lead to a stricter or looser requirement than that of surface pressure considerations alone, which would indicate about a 0.1 % precision for 1mb accuracy. Furthermore, the less sensitive the $CO_2$ measurement is to surface pressure errors, the more difficult it will be for an $O_2$ observation to provide a useful measurement.

## 1 Introduction

The present surface-based network of observing systems has been shown to be inadequate for reducing uncertainty in surface flux estimates of $CO_2$ at all but the coarsest spatial scales (Houweling et al., 2004). However, other experiments with pseudo-data (e.g., Rayner and O'Brien, 2001; Houweling et al., 2004; Hungershoefer et al., 2010) suggest that column-integrated $CO_2$ mixing ratio, denoted as $XCO_2$, as retrieved from radiances measured by satellites with instruments that are sensitive to $CO_2$ absorption features, can provide enough observations with suitable precision to both improve current surface flux estimates and reduce their associated uncertainties. The Active Sensing of $CO_2$ Emissions over Nights, Days and Seasons (ASCENDS) mission will make $CO_2$ measurements with high precision and low bias (ASCENDS Workshop Report, 2008) in order to provide retrievals of $XCO_2$ with errors in the 1–2 ppm range, which is thought necessary to constrain global sources and sinks at the regional scale (Miller et al., 2007).

Satellites measure the top-of-atmosphere radiance, which is sensitive to the integrated amount of absorbing tracer along the photon path. This amount may change with either changes in mixing ratio or of the mass of air through which photons pass. Source–sink processes only change mixing ratio. Thus, for best use in flux inversions, retrievals of $XCO_2$ require an estimate of surface pressure $p^*$ to convert the gas number density of $CO_2$ in the column to a dry air mixing ratio. Two options have been proposed for providing the $p^*$ estimate for ASCENDS, for which the $CO_2$ column number density would be retrieved using a laser differential absorption spectrometer (LAS). The first is to use the collocated value of surface pressure derived from numerical weather prediction (NWP) models. The second, and more expensive, is to employ a LAS to measure absorption in an $O_2$ band and utilize the near-constant $O_2$ mixing ratio to retrieve a robust estimate of the local surface pressure. It is reasonable to ask whether the potentially reduced errors in surface pressure provide improvements to the retrieved mixing ratios and resulting flux estimates that justify the cost of the active measurement of $O_2$, especially given the fact that active measure-

ments of $O_2$ lag the current state of the art for $CO_2$ (James Abshire, personal communication, 2014). The authors note that this need for a surface pressure estimate is not unique to active measurements. Both GOSAT and OCO-2 have detectors in $O_2$ absorption bands, and these are used to some extent to retrieve surface pressure, although they are also used for cloud and aerosol screening (e.g., Taylor et al., 2012).

In Zaccheo et al. (2014), the authors set out to quantify the impact of atmospheric state variables, such as temperature ($T$), relative humidity (RH) and surface pressure ($p^*$) on retrievals of $XCO_2$. This was accomplished by comparing weather model forecasts to collocated surface and upper-air observations and using the Line-By-Line Radiative Transfer Model (LBLRTM; Clough et al., 2005) to compute the differences in optical depth (OD) arising from the different estimates of $T$, RH and $p^*$, treated as noise, as well as from perturbations to the $CO_2$ profile and to the surface pressure for the $O_2$ measurement, which were treated as signal. The signal and noise were computed for a wide range of different absorption lines, with the conclusion that atmospheric state uncertainties propagate to at least 0.2 ppm addition to the $XCO_2$ uncertainty budget, though these numbers are highly variable depending on the lines selected.

In this paper, we present a methodology to partially answer the question of cost versus benefit for an active $O_2$ measurement by determining whether the observations of $CO_2$ mixing ratio with the active $O_2$ measurement contain more information than the NWP prediction on the *model profile* of $CO_2$, denoted $q_{CO_2}(p)$, and hence the most information on the surface fluxes in a transport model inversion. Specifically, we seek to provide an upper bound on the signal-to-noise ratio (SNR) of the $O_2$ measurement, beyond which the cost of the measurement would not be justifiable. In this work, we utilize some of the analysis in Zaccheo et al. (2014), including the matched pairs of $T$, RH and $p^*$ to compute the error standard deviations for those quantities and to include those uncertainties in computations of information content for observations with and without an active $O_2$ measurement. There are a few key differences between this work and that Zaccheo et al. (2014), though they are addressing related questions. First, we are interested in the contribution of an $O_2$ lidar but only relative to the scenario in which no such lidar is flown. That is, we are not attempting to provide estimates of errors in $XCO_2$ that arise from each of these scenarios. Secondly, we do not compute $XCO_2$ explicitly, as it introduces extra uncertainty into the problem through division by quantities that are uncertain, such as the differential absorption cross section and specific humidity. Thirdly, our method utilizes analytic expressions for the derivatives of various quantities rather than the perturbation method utilized in Zaccheo et al. (2014), which allows us to perform our analysis for many error scenarios and reference states. In principle, this analysis could be carried out similarly for any collocated observations.

The paper is laid out as follows. Section 2 defines the observations of interest and relevant terminology. In Sect. 3, the notion of Fisher information is introduced, and the relevant form used in our methodology is discussed. The error components are defined in Sect. 4. These errors, together with the derivative of the observation operators with respect to the $q_{CO_2}$ in each model layer, are used to calculate the information in each observation as functions of a few parameters related to observational errors and NWP model surface pressure errors. A SNR (precision) requirement for the usefulness of an $O_2$ measurement is derived in Sect. 3.4 and computed in Sect. 5 for the $O_2$ error for different magnitudes of surface pressure error.

## 2 Differential absorption lidar measurements

LAS instruments measure the difference in transmitted/received energies at two or more wavelengths (which for the two-line case we call "$T_{on}$" and "$T_{off}$"). $T_{on}$ is transmission on a wavelength absorbed by $CO_2$ while $T_{off}$ is on a line not subject to absorption by $CO_2$ . We denote the logarithm of the ratio as $\Delta\tau$, the differential optical depth (DOD). That is,

$$\Delta\tau_{CO_2} := -\log\left[\frac{T_{on}}{T_{off}}\right] = \int_0^{p^*} \frac{q_{CO_2}(p)\Delta\xi_{CO_2}(p)}{m_d g(p)(1+q_{H_2O}(p)\frac{m_{H20}}{m_d})}\mathrm{d}p, \quad (1)$$

where $m_d$ is the molecular mass of dry air, $m_{H_2O}$ is the molecular mass of water, $q_{H_2O}(p)$ is the dry air mixing ratio of water, $g$ is gravitational acceleration and $\Delta\xi_{CO_2}$ is the differential absorption cross section at pressure altitude $p$. This definition follows immediately from Beer's Law, which states that the transmission is given by

$$T = \exp\left[-\int_{R_1}^{R_2} n_{gas}(r)\xi_{gas}(r)\mathrm{d}r\right],$$

with $n_{gas}$ being the number density of the gas and $r$ denoting the path traversed by the laser. Note that we could reformulate these definitions in terms of geometric height $z$ in the case that this is more convenient, since the lidar also provides this measurement through ranging. Since the actual quantities measured by the instrument are $T_{on}$ and $T_{off}$, the quantity $\Delta\tau_{CO_2}$ is the most direct link between the actual observation and the model profile $q_{CO_2}(p)$, assuming that $p^*$ and $\Delta\xi_{CO_2}$ are known. The derivative of $\Delta\tau_{CO_2}$ (or $\Delta\tau_{O_2}$) per unit $q_{CO_2}$ ($q_{O_2}$) as a function of the vertical coordinate (here $p$) will be referred to as the vertical weighting function (WF):

$$W_\times(p) = \frac{\Delta\xi_\times(p)}{m_d g(p)(1+q_{H_2O}(p)\frac{m_{H20}}{m_d})}, \quad (2)$$

where $\times$ is either $CO_2$ or $O_2$. This function tells us what portion of the vertical column is providing the most weight to the retrieval of column integrated $CO_2$ or $O_2$. From Eq. (1) we can see that the WF is just $\Delta\xi_{CO_2}$ or $\Delta\xi_{O_2}$ normalized by $m_d$ and $g$.

The observation operator maps the model state ($q_{CO_2}$) into the space where the observations lie. The candidate observations in this document are the differential optical depth for $CO_2$ (using NWP $p^*$), $\Delta\tau_{CO_2}$, given in Eq. (1), and the ratio $\frac{\Delta\tau_{CO_2}}{\Delta\tau_{O_2}}$, which is written explicitly as

$$\frac{\Delta\tau_{CO_2}}{\Delta\tau_{O_2}} = \frac{\int_0^{p^*} q_{CO_2}(p) W_{CO_2}(p)}{\int_0^{p^*} q_{O_2} W_{O_2}(p) \mathrm{d}p}. \quad (3)$$

Note that the ratio $\frac{\Delta\tau_{CO_2}}{\Delta\tau_{O_2}}$ resembles (modulo the different WFs) the ratio $\frac{q_{CO_2}}{q_{O_2}}$ and so can be thought of as a surrogate for $XCO_2$, with appropriate scaling for the abundance of $O_2$ in the atmosphere. $XCO_2$ is not considered explicitly in this treatment, because it is not directly tied to the quantities measured or to the model profile of mixing ratio. In practice, inverse calculations ingest $XCO_2$, and we assume that the total information on model mixing ratio is the same whether we ingest the direct measurements of differential optical depth (with an online computation for $W$) or retrieve $XCO_2$ and $W$ offline and ingest them separately.

For ASCENDS, three candidate spectral lines have been identified as having the most potential for estimating absorption due to $CO_2$ (ASCENDS Workshop Report (2008)): two lines in the weak $CO_2$ band near 1.571 and 1.572 µm and the strong $CO_2$ band near 2.06 µm. To accompany these measurements and convert them to $XCO_2$, two oxygen measurements have been proposed: one in the oxygen A band near 0.76 µm and the other near 1.26 µm (ASCENDS Workshop Report, 2008).

The online and offline wavelengths are chosen with consideration of the sensitivity of transmission to atmospheric temperature, water vapor and pressure, since variability in these quantities will contribute to the overall uncertainty in the retrieved gas number densities. For example, Abshire et al. (2014) and Riris et al. (2013) specify the interest in the 1.572 and 0.76 µm region for $CO_2$ and $O_2$, respectively, for decreased sensitivity in absorption to temperature fluctuations.

Figure 2, which is described in greater detail in Sect. 4.2.2, shows typical vertical WFs for these spectral lines for few different choices of online wavelength. By specifying a different offset (3 or 10 pm), the layer of the atmosphere to which the measurement is most sensitive is varied. The value of $\Delta\tau_{CO_2}$ arising from the 1.571 µm–3 pm online wavelength is more indicative of the composition near the top of the troposphere, because the online wavelength is closer to line center than that of the 10 pm offset, which peaks closer to the surface. The 2.051 µm $\Delta\tau_{CO_2}$ is more indicative of values near the surface due to the stronger absorption in the strong $CO_2$ band that allows an online wavelength further from the center of the absorption feature.

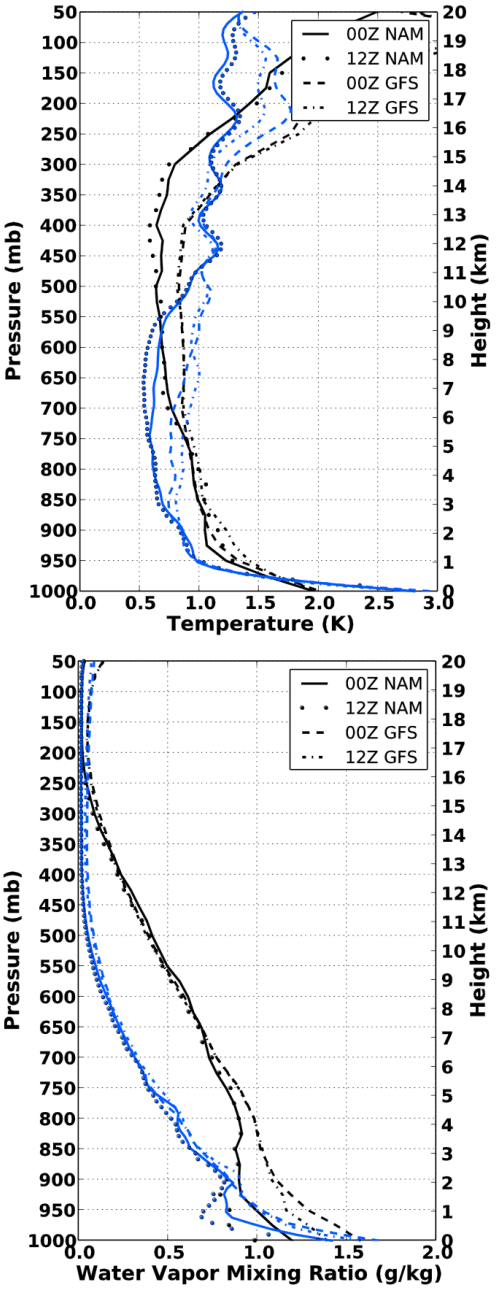


**Figure 1.** From Zaccheo et al. (2014). Ensemble RMS differences between RAOB measurements and corresponding NWP analysis temperature (top) and water vapor mixing ratio (bottom) profiles. Each panel illustrates the errors for 0Z and 12Z NWP analysis fields, respectively. The black lines represent the respective RMS differences as a function of pressure and the blue lines denote the RMS as a function of vertical height from the surface.

## 3 Information content

From (Rodgers, 2000), the Fisher information for the linearized retrieval problem with Gaussian error statistics is given by

$$\mathbf{I} = \mathbf{H}^T \mathbf{R}^{-1} \mathbf{H} + \mathbf{B}^{-1}, \tag{4}$$

where $\mathbf{R}$ is the observation error covariance matrix, $\mathbf{B}$ is the prior error covariance matrix and $\mathbf{H}$ is the Jacobian of the observation operator $\mathbf{h}$ that transforms model variables into observations. The Fisher information can be thought of as the information in the observation or retrieval about the input parameters, which compose the domain of $\mathbf{h}$, and is simply the inverse of the posterior error covariance matrix.

For the observation operators in Eqs. (1–3), the predicted quantity is a scalar $h$, meaning that its gradient (with respect to each variable) $\mathbf{H}$ is a column vector. Assuming that the prior information on $q_{CO_2}$ is the same for each candidate observable (i.e., they assume the same error statistics), this suggests that the scalar quantity

$$I_{q_{CO_2}} = \mathbf{H}_{q_{CO_2}}^T \mathbf{R}^{-1} \mathbf{H}_{q_{CO_2}} \tag{5}$$

provides a measure of a particular observable's information content on the model profile of $CO_2$. Here, $\mathbf{H}_{q_{CO_2}}$ is the Jacobian (or gradient) of $h$ with respect to the $n_{\text{layers}}$ model layer mixing ratios $[q^1_{CO_2}, \ldots, q^{n_{\text{layers}}}_{CO_2}]$, and so the quantity $\sqrt{I_{q_{CO_2}}}$ has units $\text{ppm}^{-1}$ regardless of the units of $h$. This quantity thus provides a useful manner in which to compare the utility of very different observations. It should be noted that the Jacobian $\mathbf{H}_{q_{CO_2}}$ is expensive to estimate for passive measurements (e.g., using a finite difference approximation) but is quite simple to compute analytically in the case of a lidar measurement, by simply differentiating Eqs. (A1) and (A2) (the discrete versions of Eqs. (1) and (3) with respect to the layer mixing ratios $q^i_{CO_2}$) to yield Eqs. (A3) and (A4). It remains to compute $\mathbf{R}$, which is described in detail in Sect. 4.

$I_{q_{CO_2}}$ combines the effects of the sensitivity (i.e., the derivative) of an observation to $q_{CO_2}$ with noise (i.e., the error statistics encapsulated in $\mathbf{R}$). In this way, by using $I_{q_{CO_2}}$ as a metric we follow a balanced approach to decide the most useful error requirements.

### 3.1 Sources of error

For a linear retrieval, the matrix $\mathbf{R}$ characterizes the uncertainty present in the model's predicted value of the observation as well as the observed value itself (Tarantola, 2005). As such, $\mathbf{R}$ is a combination of instrument precision (i.e., signal to noise), the uncertainty in the simulated/retrieved external quantities (such as surface pressure, temperature and moisture) and the uncertainty from things that are not explicitly modeled, such as errors in spectroscopy. The first source is treated as random error with known statistics computed from the signal-to-noise ratios. The second source includes surface pressure errors and errors in the calculated WF ($\Delta\xi_{CO_2}$) due to misspecification of local temperature and water vapor, on which the WF calculation strongly depends. The third category of errors is assumed to be negligible since we assume that transmission in nearby wavenumbers differs only in the gas absorption, and so all other effects vanish when we take the difference. This is the typical assumption for DIAL-type instruments and indeed the inspiration for the DIAL concept.

Assuming a single sounding in the retrieval (or spatially uncorrelated errors), $\mathbf{R}$ is a constant $\sigma^2(h)$, and hence $I_{q_{CO_2}} = |\mathbf{H}|^2 \sigma^{-2}(h)$. The variance $\sigma^2(h)$ is decomposed based on the considerations in the previous paragraph as

$$\sigma^2(h) = \sigma^2_{p^*}(h) + \sigma^2_{\Delta\xi}(h) + \sigma^2_{\text{obs}}(h), \tag{6}$$

where $h$ is either $\Delta\tau_{CO_2}$ or $\frac{\Delta\tau_{CO_2}}{\Delta\tau_{O_2}}$. The $h$ dependence is included to emphasize the variability of the observation $h$ due to errors in surface pressure, the weighting function (arising from errors in temperature and humidity) and instrument noise. Thus the information in a single measurement on the co-located model $q_{CO_2}$ is $\sigma^{-2}(h)|\mathbf{H}_{q_{CO_2}}|^2$, which suggests that the $i$th component of $\sigma^{-1}(h)\mathbf{H}_{q_{CO_2}}$ will represent the information in the observable about the model's $i$th layer $CO_2$ mixing ratio.

In Sects. 4.2 and 4.3 we make use of the uncertainty propagation formula, which says that if $y = h(x)$ and $\mathbf{H} = \nabla h$, then

$$\mathbf{R}_y = \mathbf{H}^T \mathbf{R}_x \mathbf{H}, \tag{7}$$

where $\mathbf{R}_x$ and $\mathbf{R}_y$ are the covariance matrices of $x$ and $y$, respectively. We use it here to connect the uncertainties in the ratio $\frac{\Delta\tau_{CO_2}}{\Delta\tau_{O_2}}$ to $\Delta\tau_{CO_2}$ and $\Delta\tau_{O_2}$, the error variances of which are given by Eq. (6). The details of these calculations for the atmospheric state induced errors are discussed in Sect. 4.

### 3.2 The observational error variance $\sigma^2_{\text{obs}}(h)$

The observed differential absorptions $\Delta\tau$ contain an instrument specific level of precision, controlled by the laser power and detector sensitivity, which we refer to as $\sigma^2_{\text{obs}}(h)$. This is typically quantified by the lab that builds and tests the instrument in a controlled environment. The ratio observable has "noise" defined as the propagation of the noise from the $CO_2$ and $O_2$ instruments (assuming no correlations between the two DOD measurement errors):

$$\sigma^2_{\text{obs}}\left(\frac{\Delta\tau_{CO_2}}{\Delta\tau_{O_2}}\right) = \Delta\tau_{O_2}^{-2}\sigma^2_{\text{obs}}(\Delta\tau_{CO_2}) + \Delta\tau^2_{CO_2}\Delta\tau_{O_2}^{-4}\sigma^2_{\text{obs}}(\Delta\tau_{O_2}). \tag{8}$$

By controlling the size of the individual lidar instruments' noise, we control the contribution to the overall error, and thus we would expect that a smaller error in one of the instruments would allow a more relaxed requirement on the

other, keeping the error budget for $XCO_2$ fixed. However, increasing precision has an added cost (e.g., associated with increasing laser power or developing more sensitive detectors) which cannot be left out of cost–benefit analyses used in decision making.

### 3.3 The total error variance for $\Delta\tau_{CO_2}$ and $\frac{\Delta\tau_{CO_2}}{\Delta\tau_{O_2}}$

In order to compute the information in each observation we summarize the preceding subsections in terms of expressions for the total uncertainty in each observation, which is just the sum of the three components described at length above.

For $\Delta\tau_{CO_2}$, assuming an estimate of $p^*$ from a NWP model, and using the expressions Eqs. (A5) and (A7), we have

$$\begin{aligned}\sigma^2(\Delta\tau_{CO_2}) &= \sigma^2_{p^*}(\Delta\tau_{CO_2}) + \sigma^2_{\Delta\xi}(\Delta\tau_{CO_2}) + \sigma^2_{\text{obs}}(\Delta\tau_{CO_2}),\\ &= (q^1_{CO_2} W^1_{CO_2})^2 \sigma^2_{\text{NWP}}(p^*) +\\ &+ \nabla_{W_{CO_2}}(\Delta\tau_{CO_2})^T \mathbf{R}_{\Delta\xi_{CO_2}} \nabla_{W_{CO_2}}(\Delta\tau_{CO_2}) +\\ &+ \sigma^2_{\text{obs}}(\Delta\tau_{CO_2}),\end{aligned} \tag{9}$$

where $\nabla_{W_{CO_2}}(\Delta\tau_{CO_2})$ is a vector of length $n_{\text{layers}}$ whose entries are given by Eq. (A7).

Similarly, for $\frac{\Delta\tau_{CO_2}}{\Delta\tau_{O_2}}$ we use the expressions Eqs. (A6), (A8) and (A9) to define

$$\begin{aligned}\sigma^2\left(\frac{\Delta\tau_{CO_2}}{\Delta\tau_{O_2}}\right) &= \sigma^2_{p^*}\left(\frac{\Delta\tau_{CO_2}}{\Delta\tau_{O_2}}\right) + \sigma^2_{\Delta\xi}\left(\frac{\Delta\tau_{CO_2}}{\Delta\tau_{O_2}}\right) +\\ &+ \sigma^2_{\text{obs}}\left(\frac{\Delta\tau_{CO_2}}{\Delta\tau_{O_2}}\right),\\ &= \left(\frac{q^1_{CO_2} W^1_{CO_2}}{\Delta\tau_{O_2}} - \frac{\Delta\tau_{CO_2}}{\Delta\tau^2_{O_2}} q^1_{O_2} W^1_{O_2}\right)^2 \sigma^2_{\text{NWP}}(p^*) +\\ &+ \nabla_W \left(\frac{\Delta\tau_{CO_2}}{\Delta\tau_{O_2}}\right)^T \mathbf{R}_{\Delta\xi} \nabla_W \left(\frac{\Delta\tau_{CO_2}}{\Delta\tau_{O_2}}\right) +\\ &+ \Delta\tau^{-2}_{O_2}\sigma^2_{\text{obs}}(\Delta\tau_{CO_2}) + \Delta\tau^2_{CO_2}\Delta\tau^{-4}_{O_2}\sigma^2_{\text{obs}}(\Delta\tau_{O_2}),\end{aligned} \tag{10}$$

where $\nabla_W\left(\frac{\Delta\tau_{CO_2}}{\Delta\tau_{O_2}}\right)$ is a vector of length $2 \times n_{\text{layers}}$, whose entries are derived from Eqs. (A8) and (A9).

### 3.4 An information-based $O_2$ requirement

In Sect. 4, the process of computing scalar error statistics $\sigma^2(h)$ for $\Delta\tau_{CO_2}$ and $\frac{\Delta\tau_{CO_2}}{\Delta\tau_{O_2}}$, which assumes no correlations between the from errors in temperature, water vapor and pressure is described. In the case of differential absorption lidar observables, we have simple analytical expressions for $h$, assuming knowledge of the surface pressure $p^*$ and the weighting function, and so the Jacobian $\mathbf{H}_{q_{CO_2}}$ can be calculated directly using Eqs. (A3) and (A4). Using these two pieces, we can compute $I_{q_{CO_2}}$ for $\Delta\tau_{CO_2}$ and $\frac{\Delta\tau_{CO_2}}{\Delta\tau_{O_2}}$.

A minimum requirement for the $O_2$ lidar investment to be cost effective is that the information in the ratio observable in Eq. (3) is greater than the $CO_2$-only observation, stated as

$$\frac{\left|\nabla_{qCO_2}\Delta\tau_{CO_2}\right|^2}{\sigma^2(\Delta\tau_{CO_2})} \leq \frac{\left|\nabla_{qCO_2}\frac{\Delta\tau_{CO_2}}{\Delta\tau_{O_2}}\right|^2}{\sigma^2\left(\frac{\Delta\tau_{CO_2}}{\Delta\tau_{O_2}}\right)}. \tag{11}$$

Noting that $\frac{\partial\Delta\tau_{CO_2}}{\partial q^i_{CO_2}} = \Delta\tau^2_{O_2}\frac{\partial}{\partial q^i_{CO_2}}\frac{\Delta\tau_{CO_2}}{\Delta\tau_{O_2}}$ yields the requirement

$$\sigma^2\left(\frac{\Delta\tau_{CO_2}}{\Delta\tau_{O_2}}\right) \leq \frac{\sigma^2(\Delta\tau_{CO_2})}{\Delta\tau^2_{O_2}}. \tag{12}$$

Expanding the error variances using Eqs. (9) and (10) and solving for $\sigma_{\text{obs}}(\Delta\tau_{O_2})$, we arrive at

$$\begin{aligned}\frac{\sigma^2_{\text{obs}}(\Delta\tau_{O_2})}{\Delta\tau^2_{O_2}} &\leq \frac{\sigma^2_{\Delta\xi}(\Delta\tau_{CO_2})}{\Delta\tau^2_{CO_2}} - \frac{\sigma^2_{\Delta\xi}\left(\frac{\Delta\tau_{CO_2}}{\Delta\tau_{O_2}}\right)}{\left(\frac{\Delta\tau_{CO_2}}{\Delta\tau_{O_2}}\right)^2} +\\ &+ \frac{\sigma^2_{p*}(\Delta\tau_{CO_2})}{\Delta\tau^2_{CO_2}} - \frac{\sigma^2_{p^*}\left(\frac{\Delta\tau_{CO_2}}{\Delta\tau_{O_2}}\right)}{\left(\frac{\Delta\tau_{CO_2}}{\Delta\tau_{O_2}}\right)^2}.\end{aligned} \tag{13}$$

Note the lack of the observational error term for $\Delta\tau_{CO_2}$ on the right-hand side of Eq. (13), meaning that the $O_2$ upper bound for usefulness is *independent of $CO_2$ precision*. Also note that this quantity will only be meaningful if

$$\frac{\sigma^2_{\Delta\xi}(\Delta\tau_{CO_2}) + \sigma^2_{p*}(\Delta\tau_{CO_2})}{\sigma^2_{\Delta\xi}\left(\frac{\Delta\tau_{CO_2}}{\Delta\tau_{O_2}}\right) + \sigma^2_{p^*}\left(\frac{\Delta\tau_{CO_2}}{\Delta\tau_{O_2}}\right)} \geq \Delta\tau^2_{O_2}, \tag{14}$$

which says that the ratio of the errors between the $\Delta\tau_{CO_2}$ and $\frac{\Delta\tau_{CO_2}}{\Delta\tau_{O_2}}$ must be greater than the $O_2$ signal. Otherwise, the right-hand side of Eq. (13) would be negative, and so no SNR would yield a useful $O_2$ measurement due to one of the sources of error in the ratio measurement being too large.

For a given choice of $CO_2$ and $O_2$ lines, the right-hand side of Eq. (13) depends solely on the expected error in surface pressure that arises from using an NWP estimate of $p^*$ in place of the true value, denoted $\sigma^2(p^*)$.

## 4 Uncertainty quantification for ASCENDS instrument concepts

In the following subsections, we outline the procedure for computing the uncertainties in the observations $\Delta\tau_{CO_2}$ and $\frac{\Delta\tau_{CO_2}}{\Delta\tau_{O_2}}$ for wavenumbers that are of interest to ASCENDS. These uncertainties are then used in Sect. 5 to seek viable $O_2$ lidar candidates that can add to the information on model $CO_2$ to better constrain flux inversions. Throughout we will use the notion of *relative uncertainty* that uses the relation Eq. (12) to suggest that we compare $\sigma^2_{(\cdot)}(\Delta\tau_{CO_2})$ and $\Delta\tau^2_{O_2}\sigma^2_{(\cdot)}\left(\frac{\Delta\tau_{CO_2}}{\Delta\tau_{O_2}}\right)$, where $(\cdot)$ is $p^*$ or $\Delta\xi$.

### 4.1 Observed and NWP-predicted variables

Atmospheric state uncertainties were computed from an extensive set of observation and model prediction pairs derived from surface weather observation station reports (METAR/SYNOP) (US DOC/NOAA OFCM, 2005) and NWP model fields collected both over the continental United States of America as well as on a global basis for representative periods between July 2011 and July 2012. The representative time periods were chosen to include data from all seasons as well as both daytime and nighttime observations. The surface observations were obtained from publicly available sources and the matching model data were extracted from both the 12 km North American Mesoscale model (NAM) (Rogers et al., 2009) and 0.5° Global Forecast System (GFS) (NCEP, 2003) analysis fields. The NAM was chosen to represent the uncertainty statistics associated with a high spatial resolution model for a well-instrumented area, and the GFS fields were chosen to illustrate the errors associated with a coarser global domain. Only 0-hour forecasts or model analysis fields were selected in this work to describe the model error characteristics based on the assumption that any operational retrieval system would either acquire data from an external source or employ an N-dimensional variational data assimilation system to minimize the impact due to uncertainties in the atmospheric state. While METAR and SYNOP are by no means an absolute representation of the atmospheric state at any point (Sun et al., 2010), they do provide a consistent measure that can be compared to NWP data for statistical purposes.

### 4.2 The environmental uncertainty contribution $\sigma^2_{\Delta\xi}(h)$

The differential absorption cross section $\Delta\xi$ is a function of the atmospheric state variables, and as such the WFs in an automated retrieval will be dynamically estimated according to local temperature ($T$), water vapor ($Q$) and pressure ($P$). The atmospheric values of $T$, $Q$ and $P$ will themselves be estimates, taken from NWP models, satellite soundings or other proxies. In order to quantify the uncertainty in the observable due to uncertainty in $\Delta\xi$, $\sigma_{\Delta\xi}(h)$, the uncertainty in $\Delta\xi$ due to uncertainty in the atmospheric state must be quantified. This analysis was carried out in a different way in Zaccheo et al. (2014), and we summarize the common methods here. The major difference is that in this work the uncertainties are propagated analytically using derivatives of the lidar observation operators, while in Zaccheo et al. (2014), the sensitivities are computed numerically using perturbations. These values should be roughly equal, but our interest lies in deriving an upper bound for $O_2$ SNR to provide a useful measurement, which is why we carry out our computations using analytic derivatives.

Sample sets of simulated absorption cross section for representative $CO_2$ absorption features at 1.571, 1.572 and 2.051 µm and $O_2$ absorption features at 0.76473 and 1.2625 µm were constructed from observed and modeled atmospheric profile data using the LBLRTM (Clough et al., 2005). The online absorption cross section values were computed for $CO_2$ at 1.571 and 1.572 µm lines with 3 and 10 pm offsets and at 2.0510 µm, at the wavenumbers currently being investigated by the ASCENDS instrument development teams. For $O_2$, the online wavelengths chosen were 0.76473 and 1.2625 µm. The offline wavelengths were chosen in a nearby region with similar characteristics for aerosols and atmospheric state variables but reduced sensitivity to absorption by $CO_2$ or $O_2$, so that the difference ($\Delta\tau$) is predominantly the signal due to the trace gas of interest. Specifically, the offline value chosen was 50 pm off the absorption feature for both weak $CO_2$ lines and the 1.2625 $O_2$ line and 100 pm off the absorption feature for the strong $CO_2$ line and the 0.76473 $O_2$ line. These offline wavelengths were selected from a range of values from 3 to 100 pm and were picked to minimize the difference between the online optical depth and the differential optical depth. The upper panel in Fig. 2 shows the WF for the online wavelength OD and the lower panel shows the WF for $\Delta\tau_{CO_2}$. The instrument WFs are qualitatively unchanged by subtracting the offline contribution, which is due to the low absorption in the offline wavelength, leading to a flat WF. Since $I_{q_{CO_2}}$ is the derivative divided by the variability, and this loss of magnitude is experienced by all realizations of the 0.76 µm WF, this difference will effectively cancel out for the purposes of computing information content.

In order to compute $\sigma_{\Delta\xi}(h)$, which we emphasize is the expected error in differential absorption cross section *due to misspecification of the atmospheric state* rather than errors in the spectroscopic characterizations of the bands of interest, we computed absorption cross sections with observed and model-predicted values of $T$, $Q$ and $P$ (described in more detail in the next paragraph) for the online and offline wavenumbers $\xi_{on}$ and $\xi_{off}$. The differential absorption cross section $\Delta\xi = \xi_{on} - \xi_{off}$. Since the vertical profiles of $\Delta\xi$ are being compared for both $CO_2$ and $O_2$, the uncertainty in the absorption cross section for an atmospheric column is most completely described by a covariance matrix $\mathbf{R}_{\Delta\xi}$ with dimensions $(2n_{layers} \times 2n_{layers})$, which includes potential correlations between errors in the WFs for $CO_2$ and $O_2$. We also point out that though we compute the covariance between errors in $T$ and $Q$, we assume that errors between these variables and surface pressure errors are uncorrelated. Also, we assume that using pressure as the vertical coordinate for $T$ and $Q$ will account for any correlations between errors in $T$ and $Q$ and the layer pressure itself.

#### 4.2.1 Compilation of $T$ and $Q$ errors

Identically to the method described in Zaccheo et al. (2014), modeled and observed atmospheric state vectors were obtained for both surface and upper-air temperature and mois-

ture. The observed profiles were derived from RAwinsonde OBservation (RAOB) observations, while model data were taken from NWP model fields. The RAOBs were obtained from publicly available sources and the matching model data were extracted from GFS (NCEP, 2003) analysis fields. RAOBs provide a consistent measure that can be compared to NWP data for statistical purposes (Sun et al., 2010). The matching NWP profiles were selected using a nearest neighbor approach based on the RAOB station location, and contained vertical temperature/moisture (RH) profiles on a fixed pressure grid and surface parameters (temperature, RH, surface pressure and station height). A conservative quality-control scheme was used to screen out RAOB with missing data and those in cloudy conditions based on the model cloud fraction and RAOB upper-air water vapor.

The standard deviation of the differences between the model-predicted $T$ and $Q$ and RAOB $T$ and $Q$ are shown in Fig. 1 for the 00:00 and 12:00 UTC soundings and for the GFS (global) and NAM (North America only) predictions. Figure 1 is identical to Fig. 1 in Zaccheo et al. (2014). Note that for the middle and lower troposphere (excluding the planetary boundary layer), $T$ differences are between 0.5 and 1.5 K for both models and times of day. Errors in $T$ are larger in the upper troposphere and in the surface layer. Differences in $Q$ as a function of height are nearly indistinguishable across models above 2 km, though their difference in pressure coordinates persists well above the planetary boundary layer. These statistics are interesting, though further investigation of their causes and implications for numerical weather prediction lie beyond the scope of this study. More details are discussed in Zaccheo et al. (2014).

#### 4.2.2 Computation of $R_{\Delta\xi}$

Layer optical depths for the desired wavenumbers, at standard layer heights between the surface and 100 km above the surface, were computed by combining the atmospheric state vectors with a nominal $CO_2$ profile with a constant vertical mixing ratio of 385 ppm to construct appropriate input parameters for the LBLRTM. The LBLRTM computes optical depths from Voigt line shape functions and a continuum model that includes self- and foreign-broadened water vapor as well as continua for carbon dioxide, oxygen, nitrogen, ozone and extinction due to Rayleigh scattering. The version employed in this study included 2012 updates to the $CO_2$ line parameters and coupling coefficients based on the work of Devi et al. (Devi et al., 2007a, b), the $O_2$ line parameters based on HITRAN (Rothman et al., 2009) and additional quadrupole parameters between 7571 and 8171 $cm^{-1}$.

Each of the 2500+ pairs of observation- and model-based weighting functions were constructed by dividing the discrete optical depth for each layer by the layer mixing ratio (i.e., 385 ppm for $CO_2$ and 209 500 ppm for $O_2$) and layer thickness given as the difference in atmospheric pressure, in accordance with the definition of weighting function in

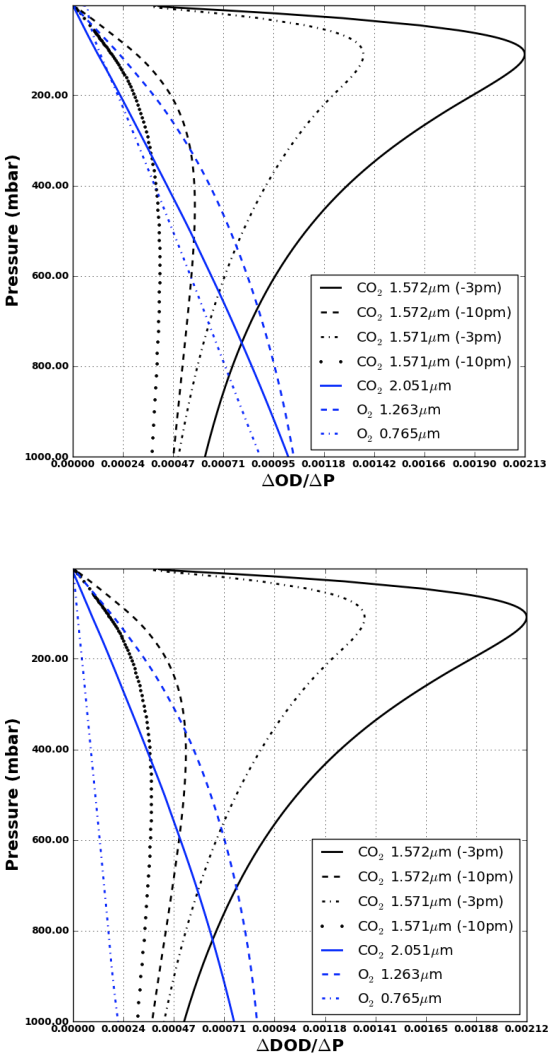


**Figure 2.** Ensemble mean weighting functions derived from NWP global vertical temperature and moisture profiles. The upper panel shows the average weighting function for the online wavelength only, and the lower plot shows the average weighting function for the differential optical depth calculation that uses an additional offline wavelength to subtract the contribution of aerosols and other scatterers. These plots show the impact of the online wavelength: the instruments sampling the 1.571 and 1.572 µm with 3 pm offset are sensitive to the top of the troposphere, while the 10 pm offset leads to sensitivity in the mid-troposphere; the 2.05 µm instrument is most sensitive near the surface, as are both $O_2$ instruments.

Eq. (2). The top panel of Fig. 2 shows the average of the ensemble set of weighting functions from the NWP-derived soundings for the OD at the online wavelength only, and the bottom panel illustrates the ensemble mean WF for the $\Delta\tau$ value, the $CO_2$ absorption features at 1.571, 1.572 µm (with online wavelengths at −3 pm and −10 pm) and 2.051 µm $CO_2$ feature and the two selected $O_2$ absorption lines at 0.76 and 1.26 µm. The offline wavelengths, which were chosen to maximize total WF signal, are 50 pm from center for the

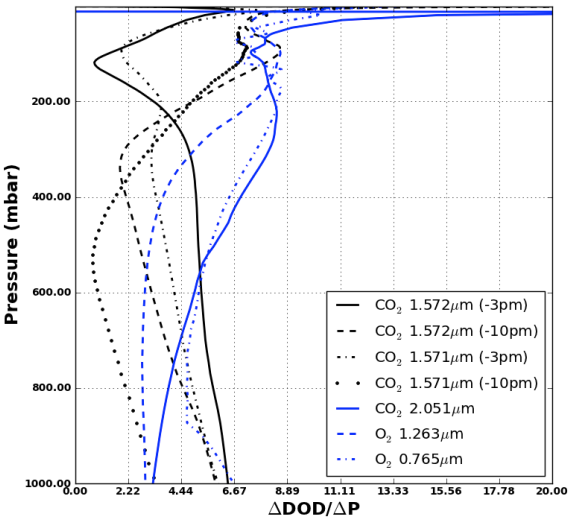


**Figure 3.** The variability in the differential optical depth weighting functions due to differences in NWP temperature and moisture as a function of vertical height. The values are the standard deviations of the difference between the average weighting function values and the ensemble members as a percentage of the mean weighting function value.

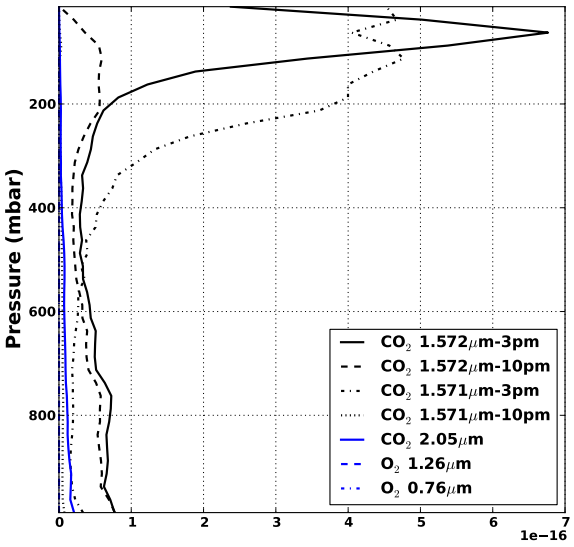


**Figure 4.** The variance of the differences between differential optical depth WFs derived from observed and modeled atmospheric soundings as a function of pressure (in 25 mb layers). The enhanced variability in the 1.571 µm–3 pm and 1.572 µm–3 pm WFs is likely due to the strong gradients in $T$ and $Q$ across the tropopause, which can be located at different heights in NWP models versus rawinsondes, as is evident from Fig. 1.

1.571 and 1.572 µm wavelengths and 1.26 µm and 100 pm from center for the 2.051 and 0.76 µm wavelengths. The subtraction of the offline OD in most of the cases has only a small effect on the total signal, with the exception of the 0.76 µm, due to the absence of aerosols in the LBLRTM calculations. In the real atmosphere, the presence of aerosols would add OD to the online and offline wavelengths in a similar way, but the DOD $\Delta\tau$ would be comprised mostly of the trace gas to the total OD measurement. Figure 3 shows the ensemble standard deviation as a percentage of the ensemble mean WF for the $\Delta\tau$ measurement, which is the variability in $\frac{\Delta\tau}{\Delta P}$ due to variations in temperature and moisture. The variability of the WFs due to $T$ and $Q$ variability is generally less than 10 % of the mean value, though there are differences between the different instruments as to where the variability is largest.

Assuming that the differences in optical depths derived from NWP and observed environments have the same distribution as the true errors, the sample error covariance $\mathbf{R}_{\Delta\xi}$ is computed by binning the differences into layers. The variance for $CO_2$ and $O_2$, as well as the in-layer covariance between $CO_2$ and $O_2$, is computed. Between-layer error correlations are assumed to be 0, which was necessary due to the heterogeneity in surface pressures (and hence the number of observations in each pressure layer) between sounding sites. The results using layer thicknesses of 25, 50 and 100 mb were examined, and there were no qualitative or quantitative differences. The results using 25 mb layers are depicted in Figs. 4 and 5. The 1.572 and 1.571 µm–3 pm variances are larger than the other instrument variances in the upper troposphere and stratosphere, which coincides with the elevated $T$ errors in Fig. 1 that are likely due to the difficulty of predicting the strong gradients across the tropopause. Since these instruments' WFs peak in this part of the atmosphere, they are the most susceptible to these errors propagating through the LBLRTM simulations. The rest of the instruments' variances fall between 0 and 1e-16, which corresponds to a standard deviation of a small fraction ($\sim 0.001$ %) of the ensemble mean values depicted in Fig. 2 once the background mixing ratio contribution from $CO_2$ or $O_2$ has been removed.

### 4.2.3 Computation of $\sigma_{\Delta\xi}(h)$

Applying Eq. (7) with the partial derivatives given by Eqs. (A7–A9) and the profiles in Figs. 4 and 5 and Eqs. (A7–A9) yields $\sigma^2_{\Delta\xi}(h)$, for which the computed values are displayed in Table 1. The magnitude of the 0.76 µm covariances shown in Fig. 5 carries through to $\sigma_{\Delta\xi}\left(\frac{\Delta\tau_{CO_2}}{\Delta\tau_{O_2}}\right)$, and the resulting values are larger than the corresponding values for the 1.26 µm ratios. Only in the 1.572 µm–10 pm:1.26 µm case is the value of $\sigma_{\Delta\xi}\left(\frac{\Delta\tau_{CO_2}}{\Delta\tau_{O_2}}\right)$ smaller as a percentage of the observation than that of $\sigma_{\Delta\xi}(\Delta\tau_{CO_2})$. This is significant because smaller errors lead to larger information content, assuming the sensitivities are comparable.

It is important to note that these computations assume a perfect radiative transfer model and as such do not contain systematic errors in the spectroscopic characterizations themselves. Quantifying the impact of such errors is beyond

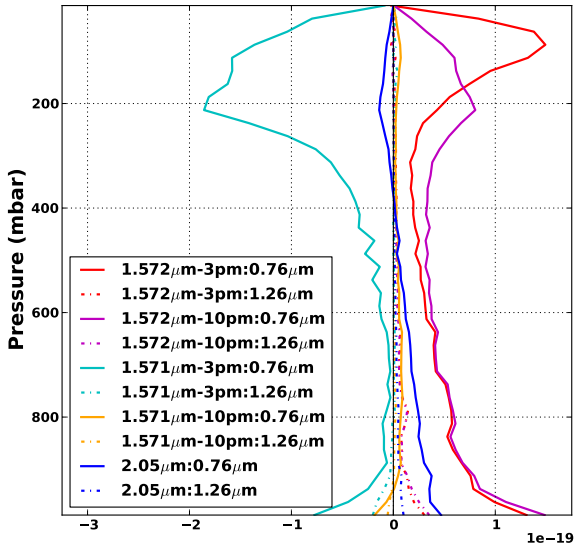


**Figure 5.** The in-layer covariance of the differences between differential optical depths derived from observed and modeled atmospheric soundings, as a function of pressure (in 25 mb layers). The covariances between the $CO_2$ instruments and the 0.76 µm are uniformly larger than those with the 1.26 µm instrument. Also, the 3 pm offset instruments have large covariances near the tropopause, which is consistent with Fig. 4.

**Table 1.** Temperature- and humidity-induced weighting function relative uncertainty for $\Delta\tau_{CO_2}$ (first column) and $\frac{\Delta\tau_{CO_2}}{\Delta\tau_{O_2}}$. The values for $\sigma_{\Delta\xi}(h)$ were computed using Eqs. (A7–A9) and the profiles in Figs. 4 and 5. The value for $\Delta\tau_{CO_2}$ is $\sigma^2_{\Delta\xi}(\Delta\tau_{CO_2})$, while for $\frac{\Delta\tau_{CO_2}}{\Delta\tau_{O_2}}$ the relative uncertainty value is $\sigma^2_{\Delta\xi}\left(\frac{\Delta\tau_{CO_2}}{\Delta\tau_{O_2}}\right)\Delta\tau^2_{O_2}$. All computations assume constant profiles of 400 ppm of $CO_2$ and 21 % of $O_2$. Note the larger magnitude of the 0.76 µm uncertainties, which arises from the larger covariances depicted in Fig. 5. Also note that only in the case of the 1.572 µm–10 pm $CO_2$ instrument paired with the 1.26 µm $O_2$ instrument is the ratio less sensitive to the environmental errors than the $\Delta\tau_{CO_2}$ measurement alone.

| $CO_2$ line | $\Delta\tau_{CO_2}$ | $O_2$ line 0.76 µm $\frac{\Delta\tau_{CO_2}}{\Delta\tau_{O_2}}$ | $O_2$ line 1.26 µm $\frac{\Delta\tau_{CO_2}}{\Delta\tau_{O_2}}$ |
|---|---|---|---|
| 1.572 µm–3 pm | 1.719e-06 | 1.182e-05 | 1.767e-06 |
| 1.572 µm–10 pm | 6.429e-07 | 1.962e-06 | 2.62e-07 |
| 1.571 µm–3 pm | 2.15e-06 | 7.481e-06 | 4.121e-06 |
| 1.571 µm–10 pm | 5.895e-08 | 8.193e-07 | 1.471e-07 |
| 2.051 µm | 1.12e-07 | 1.563e-06 | 2.5e-07 |

the scope of this paper, and we assume that the state of the art radiative transfer models will be used in any operational retrievals.

### 4.3 The surface pressure uncertainty contribution $\sigma^2_{p^*}(h)$

In the context of surface pressure errors, with scalars $h$ and $\sigma^2(p^*)$, Eq. (7) implies

$$\sigma^2_{p^*}(h) = \left(\frac{\partial h}{\partial p^*}\right)^2 \sigma^2(p^*). \quad (15)$$

Note that $\frac{\partial h}{\partial p^*}$ has been computed for $\Delta\tau_{CO_2}$ and $\frac{\Delta\tau_{CO_2}}{\Delta\tau_{O_2}}$ in Eqs. (A5–A6).

The observed surface pressure values were extracted from 107 airport and/or permanent surface weather observation station reports for the same contiguous United States (CONUS) and global regions described above along with their corresponding NWP model values. The NWP model values were corrected to the observed station height using a standard lapse rate relationship. The resulting $1\sigma$ value for the CONUS region was approximately 1.1 mbar and the $2\sigma$ value was 2.1 mbar. The global region exhibited a $1\sigma$ value of 0.8 mbar and a $2\sigma$ value of 1.7 mbar. Globally these observations showed no significant biases and only slight seasonal variation in standard deviations. An in-depth discussion of the methods (including pressure correction for terrain height versus model represented terrain height) and analysis of these values is presented in Zaccheo et al. (2014).

The values of $\sigma_{p*}(\Delta\tau_{CO_2})$ and $\Delta\tau_{O_2}\sigma_{p^*}\left(\frac{\Delta\tau_{CO_2}}{\Delta\tau_{O_2}}\right)$ are displayed in Table 2 for $\sigma_{NWP}(p^*)$ values of 1mb and 2mb. Surprisingly, in terms of relative uncertainty, the ratio observations were not uniformly less sensitive to surface pressure errors than the $\Delta\tau_{CO_2}$ observations. The two weak $CO_2$ band lidars with the 3 pm offset were actually less sensitive to surface pressure errors when no $O_2$ measurement was included. This is due to the majority of their weight being concentrated near the tropopause and hence very little information coming from the surface. By contrast, the other two weak $CO_2$ band instruments show a reduced sensitivity to errors in surface pressure from the inclusion of $O_2$ observations in the 1.26 µm regime, and the strong $CO_2$ band instrument benefits from the inclusion of either $O_2$ observation in the 0.76 µm as well as those at 1.26 µm. In parentheses is the sum of the surface pressure relative uncertainty and the WF relative uncertainty from Table 1. According to Eq. (14), the value in parentheses for $\frac{\Delta\tau_{CO_2}}{\Delta\tau_{O_2}}$ must be smaller than the value in parentheses for $\Delta\tau_{CO_2}$ in order for there to be a useful $O_2$ measurement. The values that satisfy this criterion are printed in boldface.

## 5 Information-based Precision requirements for ASCENDS

The upper bound given by Eq. (13) was computed for 1mb and 2mb values of $\sigma(p^*)$, and the results are displayed as percentages of the corresponding $\Delta\tau_{O_2}$ observations in Table 3 as well as SNR in parentheses. To first order, one would

**Table 2.** Surface pressure relative uncertainty for $\Delta\tau_{CO_2}$ and $\frac{\Delta\tau_{CO_2}}{\Delta\tau_{O_2}}$, with total environmental relative uncertainty in parentheses. The values for $\sigma_{\Delta\xi}(h)$ were computed using Eqs. (A5–A6) and $\sigma(p^*) = 1$ mb and $\sigma(p^*) = 2$ mb. The values in parentheses are the values from Table 1 added to the surface pressure relative uncertainties, and boldfaced values indicate instrument configurations for which an $O_2$ lidar with enough precision could provide more information than the $CO_2$ only configuration with NWP $p^*$. Relative uncertainties are $\sigma^2_{p^*}(\Delta\tau_{CO_2})$ and $\sigma^2_{p^*}\left(\frac{\Delta\tau_{CO_2}}{\Delta\tau_{O_2}}\right)\Delta\tau^2_{O_2}$. All computations assume constant profiles of 400 ppm of $CO_2$ and 21 % of $O_2$.

| | $O_2$ line | | | |
|---|---|---|---|---|
| $CO_2$ line | 0.76 µm | 1.26 µm | | |
| 1.572 µm–3 pm | 1.098e-06 | 1.411e-05 | 5.667e-06 | |
| | (2.818e-06) | (2.593e-05) | (7.434e-06) | |
| 1.572 µm–10 pm | 6.1e-07 | 1.2e-06 | 3.116e-07 | |
| | (1.253e-06) | (3.162e-06) | (**5.735e-07**) | |
| 1.571 µm–3 pm | 6.313e-07 | 6.325e-06 | 2.457e-06 | $\sigma(p^*) = 1$ mb |
| | (2.782e-06) | (1.381e-05) | (6.578e-06) | |
| 1.571 µm–10 pm | 3.373e-07 | 4.879e-07 | 1.104e-07 | |
| | (3.962e-07) | (1.307e-06) | (**2.575e-07**) | |
| 2.051 µm | 2.547e-06 | 5.478e-08 | 8.399e-08 | |
| | (2.659e-06) | (**1.618e-06**) | (**3.339e-07**) | |
| 1.572 µm–3 pm | 4.393e-06 | 5.642e-05 | 2.267e-05 | $\sigma(p^*) = 2$ mb |
| | (6.113e-06) | (6.824e-05) | (2.444e-05) | |
| 1.572 µm–10 pm | 2.44e-06 | 4.799e-06 | 1.246e-06 | |
| | (3.083e-06) | (6.761e-06) | (**1.508e-06**) | |
| 1.571 µm–3 pm | 2.525e-06 | 2.53e-05 | 9.829e-06 | |
| | (4.676e-06) | (3.278e-05) | (1.395e-05) | |
| 1.571 µm–10 pm | 1.349e-06 | 1.951e-06 | 4.416e-07 | |
| | (1.408e-06) | (2.771e-06) | (**5.888e-07**) | |
| 2.051 µm | 1.019e-05 | 2.191e-07 | 3.36e-07 | |
| | (1.03e-05) | (**1.782e-06**) | (**5.859e-07**) | |

expect that the $O_2$ measurement error requirement should match the pressure requirement, e.g., for a pressure error of 1 mb (about 0.1 % of a nominal 1000 mb $p^*$) we should have an $O_2$ measurement error of about 0.1 % or a SNR requirement of 1000. Table 3 shows that the impact of including the environmentally induced errors as part of the calculation depends on the wavelengths of the $CO_2$ and $O_2$ instruments.

The 0.76 µm $O_2$ instrument column is N/A for each of the pairings with the weak band $CO_2$ instruments, indicating that no precision would be sufficient to provide a ratio measurement that improves on $\Delta\tau_{CO_2}$ with NWP $p^*$. This is largely due to the larger errors in the corresponding $\frac{\Delta\tau_{CO_2}}{\Delta\tau_{O_2}}$ observation due to uncertainties in temperature and water vapor. The 0.76 µm $O_2$ measurement does have the potential to improve upon the strong band $CO_2$-only measurement, which is due to the large sensitivity of the 2.051 µm instrument to surface pressure errors. This is evident in the fact that the doubling of surface pressure error from 1 to 2 mb relaxes the $O_2$ precision requirement by nearly a factor of 3. Hence the environmental error contribution in the 0.76 µm line is overwhelmed by the surface pressure errors for the 2.051 µm line.

Examining the column for the 1.26 µm line we see that the smaller sensitivities to temperature and water vapor errors increase the potential for improvement on two of the weak $CO_2$ band instruments, namely those with the 10 pm offset. In this case, the surface pressure errors in these $CO_2$ only observations are large enough to offset the total errors in the ratio observations. For the 1.572 µm : 1.26 µm ratio, noted before because the ratio's environmental errors are actually smaller than those of the $CO_2$ only observation, the minimum precision is smaller than that of the 1.571 µm ratio (i.e., SNR of 1087 vs. 1642 for 1 mb surface pressure errors). Doubling the surface pressure error again increases the precision but not by as large a factor as in the 0.76 µm case. This is not surprising, because the ratios using the 0.76 µm line have larger sensitivities to surface pressure, as is evident in Table 2.

Perhaps most surprising is that our analysis concludes that neither $O_2$ measurement provides useful information to the 1.571 µm–3 pm or 1.572 µm–3 pm lines. This is due to the fact that these instruments are relatively insensitive to surface pressure errors due to their weighting function shapes. Thus, providing a high SNR $O_2$ measurement would have a negative impact on their total uncertainty budget due to the addition of environmental errors that come from using erroneous temperature and water vapor profiles in the WF estimation.

**Table 3.** Upper bounds on the $O_2$ measurement uncertainty $\sigma_{obs}(\Delta\tau_{O_2})$ computed from Eq. (13) expressed as percentages of a representative $\Delta\tau_{O_2}$ using 21 % atmospheric concentration and a typical vertical WF. The corresponding SNR lower bound is given in parentheses. For example, if the surface pressure error is 1 mb, the 0.76 µm precision would have to be smaller than 0.1167 % in order for the ratio with the strong band $CO_2$ measurement to provide a better constraint on model $CO_2$ than the $CO_2$ measurement alone using NWP $p^*$. The quantity N/A represents the scenarios in which Eq. (13) yielded a negative number, i.e., in which no $O_2$ instrument precision would yield a larger information content on model $q_{CO_2}$ than the corresponding $\Delta\tau_{CO_2}$ measurement using NWP $p^*$.

| | $O_2$ line | | |
|---|---|---|---|
| $CO_2$ line | 0.76 µm | 1.26 µm | |
| 1.572 µm–3 pm | N/A | N/A | $\sigma(p^*) = 1$ mb |
| 1.572 µm–10 pm | N/A | 0.0920 (1087) | |
| 1.571 µm–3 pm | N/A | N/A | |
| 1.571 µm–10 pm | N/A | 0.0609 (1642) | |
| 2.051 µm | 0.1167 (857) | 0.1745 (573) | |
| 1.572 µm–3 pm | N/A | N/A | $\sigma(p^*) = 2$ mb |
| 1.572 µm–10 pm | N/A | 0.1400 (714) | |
| 1.571 µm–3 pm | N/A | N/A | |
| 1.571 µm–10 pm | N/A | 0.1481 (675) | |
| 2.051 µm | 0.3339 (300) | 0.3566 (280) | |

## 6 Conclusions

The preceding work defines an information-based measurement precision requirement for an $O_2$ instrument to provide additional information on column $CO_2$ above and beyond a $CO_2$ measurement taken together with an NWP prediction of surface pressure. The requirement includes the impacts of environmentally induced WF error correlations between the $O_2$ and $CO_2$ measurements as well as the expected variability of each due to surface pressure errors. Tests were performed using proxies for errors in the atmospheric state taken from NWP predictions and RAOBs for two different candidate $CO_2$ and $O_2$ spectral lines. The major finding is that for NWP surface pressure errors in the expected range of 1 to 2 mb Zaccheo et al. (2014), the contribution of the environmental uncertainty to the overall measurement requirement cannot be excluded in design considerations since for the 0.76 µm case these errors actually disqualified the instrument from being useful in conjunction with any weak $CO_2$ band lidar. The 1.26 µm instrument has more options for pairings but with smaller precision than would be expected from a pressure requirement alone for the weak $CO_2$ band. Both instruments do show the potential for providing additional information on the 2.051 µm line, at a more relaxed precision requirement than the pressure would suggest. This is due to the reduced sensitivity of the ratio observations to surface pressure errors over the $CO_2$ observations alone.

The authors realize that we have only explored a small set of candidate wavelengths in the spectral bands of interest. We stress, however, that we are exploring exactly those lines being targeted by current ASCENDS instrument design teams. It is beyond the scope of this paper to provide a complete characterization of all $CO_2$ and $O_2$ absorption figures. In the event that other spectral lines are considered, this analysis will be repeated.

In the context of ever improving global NWP models, it is important to note that we expect global NWP surface pressure errors to trend toward the lower end of our $\sigma(p^*)$ spectrum, which is 1mb or less. This being the case, justifying the expense for an active $O_2$ measurement can be expected to become more difficult the longer that ASCENDS or other similar systems are delayed from launching. Tightening the precision of the lidar becomes more difficult and expensive the more accurate that NWP models become. It seems that the best option to avoid sensitivity to surface pressure errors is either a weak $CO_2$ band lidar with NWP atmospheric variables or a strong $CO_2$ band lidar paired with either of these two $O_2$ lidars.

*Acknowledgements.* Crowell would like to acknowledge grant support from NASA Headquarters and the Langley Research Center (NASA). Rayner is in receipt of an Australian Professorial Fellowship (DP1096309). Zaccheo is funded in part by a grant from NASA Headquarters.

Edited by: G. Ehret

## Appendix A: Discretized operators and their derivatives

Equations Eqs. (1–3) above are two examples of **h**. In the discrete case (i.e., in a numerical model), these observation operators are expressed using sums:

$$\Delta\tau_{\mathrm{CO_2}} = \frac{1}{m_a g}\sum_{i=1}^{n_{\mathrm{layers}}} q^i_{\mathrm{CO_2}} W^i_{\mathrm{CO_2}} \Delta p^i, \tag{A1}$$

$$\frac{\Delta\tau_{\mathrm{CO_2}}}{\Delta\tau_{\mathrm{O_2}}} = \frac{\sum_{i=1}^{n_{\mathrm{layers}}} q^i_{\mathrm{CO_2}} W^i_{\mathrm{CO_2}} \Delta p^i}{\sum_{i=1}^{n_{\mathrm{layers}}} q^i_{\mathrm{O_2}} W^i_{\mathrm{O_2}} \Delta p^i}. \tag{A2}$$

The derivatives of the discrete observation operators Eqs. (A1–A2) with respect to the layer mixing ratios $q^i_{\mathrm{CO_2}}$ are given by

$$\frac{\partial \Delta\tau_{\mathrm{CO_2}}}{\partial q^i_{\mathrm{CO_2}}} = W^i_{\mathrm{CO_2}} \Delta p^i, \tag{A3}$$

$$\frac{\partial}{\partial q^i_{\mathrm{CO_2}}}\frac{\Delta\tau_{\mathrm{CO_2}}}{\Delta\tau_{\mathrm{O_2}}} = \frac{W^i_{\mathrm{CO_2}} \Delta p^i}{\sum_{j=1}^{n_{\mathrm{layers}}} q^j_{\mathrm{O_2}} W^j_{\mathrm{O_2}} \Delta p^j}. \tag{A4}$$

According to the fundamental theorem of calculus, $\frac{d}{dp^*}\int_0^{p^*} f(p)\mathrm{d}p = f(p^*)$, and so we define the derivatives of Eqs. (A1–A2) with respect to $p^*$ to satisfy this as closely as possible:

$$\frac{\partial \Delta\tau_{\mathrm{CO_2}}}{\partial p^*} = q^1_{\mathrm{CO_2}} W^1_{\mathrm{CO_2}}, \tag{A5}$$

$$\frac{\partial}{\partial p^*}\frac{\Delta\tau_{\mathrm{CO_2}}}{\Delta\tau_{\mathrm{O_2}}} = \frac{q^1_{\mathrm{CO_2}} W^1_{\mathrm{CO_2}}}{\Delta\tau_{\mathrm{O_2}}} - \frac{q^1_{\mathrm{O_2}} W^1_{\mathrm{O_2}}}{\Delta\tau_{\mathrm{O_2}}}\frac{\Delta\tau_{\mathrm{CO_2}}}{\Delta\tau_{\mathrm{O_2}}}, \tag{A6}$$

where the superscript 1 indicates the model surface layer. The derivatives of the observation operators with respect to the layer weighting functions $W^i$ are

$$\frac{\partial \Delta\tau_{\mathrm{CO_2}}}{\partial \Delta\xi^i_{\mathrm{CO_2}}} = q^i_{\mathrm{CO_2}} \Delta p^i, \tag{A7}$$

$$\frac{\partial}{\partial W^i_{\mathrm{CO_2}}}\frac{\Delta\tau_{\mathrm{CO_2}}}{\Delta\tau_{\mathrm{O_2}}} = \frac{q^i_{\mathrm{CO_2}} \Delta p^i}{\sum_{j=1}^{n_{\mathrm{layers}}} q^j_{\mathrm{O_2}} W F^j_{\mathrm{O_2}} \Delta p^j}, \tag{A8}$$

$$\frac{\partial}{\partial W^i_{\mathrm{O_2}}}\frac{\Delta\tau_{\mathrm{CO_2}}}{\Delta\tau_{\mathrm{O_2}}} = -\frac{q_{\mathrm{O_2}} \Delta p^i \sum_{j=1}^{n_{\mathrm{layers}}} q^j_{\mathrm{CO_2}} W^j_{\mathrm{CO_2}} \Delta p^j}{\left(\sum_{j=1}^{n_{\mathrm{layers}}} q_{\mathrm{O_2}} W^j \Delta p^j\right)^2}. \tag{A9}$$

## References


Abshire, J., Ramanathan, A., Riris, H., Mao, J., Allan, G., Hasselbrack, W., Weaver, C., and Browell, E.: Airborne measurements of $CO_2$ Column Concentration and Range Using a Pulsed Direct-Detection IPDA Lidar, Remote Sens., 6, 443–469, 2014.

Clough, S. et al.: Atmospheric radiative transfer modeling: a summary of the AER codes, Short Communication, J. Quant. Spectrosc. Radiat. Transfer, 91, 233–244, 2005.

Devi, V., Benner, D., Brown, L., Miller, C., and Toth, R.: Line mixing and speed dependence in $CO_2$ at 6227.9 $cm^{-1}$: constrained multispectrum analysis of intensities and line shapes in the 30013←00001 band, J. Mol. Spectrosc., 245, 52–80, 2007a.

Devi, V., Benner, D., Brown, L., Miller, C., and Toth, R.: Line mixing and speed dependence in $CO_2$ at 6348 $cm^{-1}$: positions, intensities, and air- and self-broadening derived with constrained multispectrum analysis, J. Mol. Spectrosc., 242, 90–117, 2007b.

Houweling, S., Breon, F.-M., Aben, I., Rödenbeck, C., Gloor, M., Heimann, M., and Ciais, P.: Inverse modeling of $CO_2$ sources and sinks using satellite data: a synthetic inter-comparison of measurement techniques and their performance as a function of space and time, Atmos. Chem. Phys., 4, 523–538, doi:10.5194/acp-4-523-2004, 2004.

Hungershoefer, K., Breon, F.-M., Peylin, P., Chevallier, F., Rayner, P., Klonecki, A., Houweling, S., and Marshall, J.: Evaluation of various observing systems for the global monitoring of $CO_2$ surface fluxes, Atmos. Chem. Phys., 10, 10503–10520, doi:10.5194/acp-10-10503-2010, 2010.

Miller, C. E., Crisp, D., DeCola, P. L., Olsen, S. C., Randerson, J. T., Michalak, A. M., Alkhaled, A., Rayner, P., Jacob, D. J., Suntharalingam, P., Jones, D. B. A., Denning, A. S., Nicholls, M. E., Doney, S. C., Pawson, S., Boesch, H., Connor, B. J., Fung, I. Y., O'Brien, D., Salawitch, R. J., Sander, S. P., Sen, B., Tans, P., Toon, G. C., Wennberg, P. O., Wofsy, S. C., Yung, Y. L., and Law, R. M.: Precision requirements for space-based data, J. Geophys. Res.-Atmos., 112, doi:10.1029/2006JD007659, 2007.

NASA: NASA ASCENDS Mission Science Definition and Planning Work-shop Report, Tech. rep., National Aeronautics and Space Agency, http://cce.nasa.gov/ascends/12-30-08%20ASCENDS_Workshop_Report%20clean.pdf, 2008.

NCEP: The GFS Atmospheric Model, NOAA, Washington, D.C., 2003.

Rayner, P. J. and O'Brien, D. M.: The utility of remotely sensed $CO_2$ concentration data in surface source inversions, Geophys. Res. Lett., 28, 175–178, 2001.

Riris, H., Rodriguez, H., Allan, G., Hasselbrack, W., Mao, J., Stephen, M., and Abshire, J.: Pulsed airborne lidar measurements of atmospheric optical depth using the Oxygen A-band at 765 nm, Appl. Opt., 52, 6369–6382, 2013.

Rodgers, C.: Inverse methods for atmospheric sounding, in: Atmospheric, Ocean and Planetary Physics, World Scientific, World Scientific & Co., Singapore, 1–40, 2000.

Rogers, E., DiMego, G., Black, T., Ek, M., Ferrier, B., Gayno, G., Janjic, Z., Lin, Y., Pyle, M., Wong, V., Wu, B. S., and Carley, J.: The NCEP North American Mesoscale Modeling System: Recent Changes and Future Plans, 2A.4, available at: http://ams.confex.com/ams/pdfpapers/154114.pdf (last access: 7 July 2014), 2009.

Rothman, L. S., Gordon, I. E., Barbe, A., Benner, D. C., Bernath, P. F., Birke, M., Boudon, V., Brown, L. R., Campargue, A., Champion, J.-P., Chance, K., Coudert, L. H., Dana, V., Devi, V. M., Fally, S., Flaud, J.-M., Gamachel, R. R., Goldman, A., Jacquemart, D., Kleiner, I., Lacome, N., Lafferty, W. J., Mandin, J.-Y., Massie, S. T., Mikhailenko, S. N., Miller, C. E., Moazzen-Ahmadi, N., Naumenko, O. V., Nikitin, A. V., Orphal, J., Perevalov, V. I., Perrin, A., Predoi-Cross, A., Rinsland, C. P., Rotger, M., M. Šimečková, Smith, M. A. H., Sung, K., Tashkun, S. A., Tennyson, J., Toth, R. A., Vandaele, A. C., Vander Auwera, J.: The HITRAN 2008 molecular spectroscopic database, J. Quant. Spectrosc. Ra., 110, 533–572, 2009.

Sun, B., Reale, A., Seidel, D., and Hunt, D.: Comparing radiosonde and COSMIC atmospheric profile data to quantify differences among radiosonde types and the effects of imperfect collocation on comparison statistics, J. Geophys. Res.-Atmos., 115, D23104, doi:10.1029/2010jd014457, 2010.

Tarantola, A.: Inverse Problem Theory and Methods for Model Parameter Estimation, SIAM, 2005.

Taylor, T., O'Dell, C., O'Brien, D., Kikuchi, N., Yokota, T., Nakajima, T., Ishida, H., Crisp, D., and Nakajima, T.: Comparison of Cloud-Screening Methods Applied to GOSAT Near-Infrared Spectra, IEEE T. Geosci. Remote. Sens., 50, 295–308, 2012.

US DOC/NOAA OFCM: Surface Weather Observations and Reports, available at: http://www.ofcm.gov/fmh-1/fmh1.htm (last access: 07 July 2014), 2005.

Zaccheo, T. S., Pernini, T., Snell, H. E., and Browell, E. V.: Impact of atmospheric state uncertainties on retrieved $XCO_2$ columns from laser differential absorption spectroscopy measurements, J. Appl. Remote Sens., 8, 083575, doi:10.1117/1.JRS.8.083575, 2014.